Evaluation and visualization of multiaxial stress and strain states under non-proportional loading

T. Itoh, M. Sakane
Ritsumeikan University, Japan
itohtaka@fc.ritsumei.ac.jp, sakanem@se.ritsumei.ac.jp

T. Morishita
College of Science & Engineering, Ritsumeikan University, Japan
gr0202xp@ed.ritsumei.ac.jp

ABSTRACT. This paper presents a simple method of determining stresses and strains and a severity of loading history under non-proportional loadings with defining the rotation angles of the maximum principal stress and strain in a three dimensional stress and strain space. Based on the method, non-proportional stress and strain ranges are derived and applicability of the range to the life evaluation for low carbon steel under non-proportional random strain paths are discussed. The strain range taking account of intensity of loading path reducing life can be suitable parameter for multiaxial fatigue life evaluation under multiaxial non-proportional loading. This paper also shows a method of visually presenting the principal stress and strain that assists designers to understand the loading mode whether proportional or non-proportional under 3 dimensional (6 stress/strain components) multiaxial loading.

KEYWORDS. Fatigue; Low cycle fatigue; Multiaxial loading; Non-proportional loading; Stress and strain evaluation; Random loading; Visualization of multiaxial loading.

INTRODUCTION

Most design codes use equivalent values to express the intensity of multiaxial stress or strain, like von Mises or Tresca equivalent stress and strain, and fatigue lives are usually estimated using equivalent values under multiaxial stress and strain states. The equivalent value means a scalar parameter that expresses intensity of a physical phenomenon in multiaxial stress states and should be reduced to be a uniaxial value in uniaxial stress state. Most widely used equivalent parameters are the von Mises and the Tresca equivalent stresses and strains. The von Mises equivalent stress physically expresses the intensity of shear strain energy and the Tresca equivalent stress that of the maximum shear stress. For example, ASME Section III, Division 1 NH [1] uses the von Mises equivalent strain and ASME Section VIII, Division 3 [2] the maximum shear stress. However, the von Mises equivalent stress and strain have no negative values so that they have a difficulty of expressing stress and strain ranges. The Tresca equivalent stress and strain have negative values but they also have a difficulty to put a sign to the shear stress and strain under multiaxial loading. Especially, in non-proportional loading where the principal stress and strain change their directions, giving a sign to them becomes more difficult. A simple and clear method of calculating stress and strain ranges is needed for describing multiaxial fatigue.

Low cycle fatigue (LCF) lives are reduced under strain controlled non-proportional loading accompanied by additional cyclic hardening compared with proportional loading [3-8] and an appropriate design method of evaluating the non-proportional fatigue life is needed for a reliable design and maintenance of structural components. Classical models particularly applicable in multiaxial fatigue life evaluation under proportional loadings lead to overestimate the lives under non-proportional loadings. For life evaluation under non-proportional loading, commonly proposed models are critical plane approaches that consider specific plane applied the critical damage, such as a Simith-Watoson-Topper [9] and a Fatemi-Socie [10] models. The authors also proposed a strain parameter (Itoh-Sakane model) estimating the non-proportional LCF lives for several materials under various strain histories [6, 7, 11-15]. This parameter is the strain based model with introducing two parameters, non-proportional factor and material constant. The former one reflects the intensity of non-proportional loading reducing life and the latter one is related to the material dependence for degree of life reduction due to non-proportional loading.

The Simith-Watoson-Topper, the Fatemi-Socie and the Itoh-Sakane models have been demonstrated to be applicable to life evaluation under non-proportional loading using hollow cylinder specimens in a laboratory level. That is, these models can be applicable to the life evaluation under limited non-proportional loadings such as the loadings in the plane stress state. However, many components and structures such as turbine blade, pressure vessel and pipe which receive combined thermal and mechanical loadings undergo non-proportional loading in which principal directions of stress and strain are changed into various directions under wider multiaxial stress and strain states [8, 13, 16-18]. Therefore, a development of suitable models for the design of actual components where variation in principal directions of stress and strain *vs* time is changed 3-dimensionally is required.

This study presents a method of evaluating the principal stress and strain ranges and the mean stress and strain, and also presents a method of calculating the non-proportional factor which expresses the severity of non-proportional loading in 3-dimantional (3D) stress and strain space (6 stress/strain components). Based on the method proposed, non-proportional strain and stress ranges are derived and applicability of the range to the life evaluation of type 304 stainless steel under 15 proportional and non-proportional strain paths are also discussed. This study also shows a method of visually presenting the stress/strain, the non-proportionality of loading and the damage evaluation.

STRESS AND STRAIN UNDER NON-PROPORTIONAL LOADING

Definition of stress and strain

Fig. 1 illustrates three principal vectors, $\boldsymbol{S}_i(t)$, applied to a small cube in material at time t in xyz-coordinates (spatial coordinates), where "S" is the symbol denoting either stress "σ" or strain "ε". Thus, $\boldsymbol{S}_i(t)$ are the principal stress vectors for the case of stress and are the principal strain vectors for the case of strain. The subscript, i, takes 1, 2 or 3 in descending order of principal stress or strain. The maximum principal vector, $\boldsymbol{S}_1(t)$, is defined as $\boldsymbol{S}_i(t)$ whose absolute value takes maximum one, *i.e.*, $\boldsymbol{S}_1(t)=\boldsymbol{S}_1(t)$ when $\boldsymbol{S}_1(t)$ takes maximum magnitude among $\boldsymbol{S}_i(t)$. The maximum principal value, $S_1(t)$, is defined as the maximum absolute value of $\boldsymbol{S}_i(t)$ as,

$$S_1(t) = \left|\boldsymbol{S}_1(t)\right| = \mathrm{Max}\left[\ \left|\boldsymbol{S}_1(t)\right|,\ \left|\boldsymbol{S}_2(t)\right|,\ \left|\boldsymbol{S}_3(t)\right|\ \right] \tag{1}$$

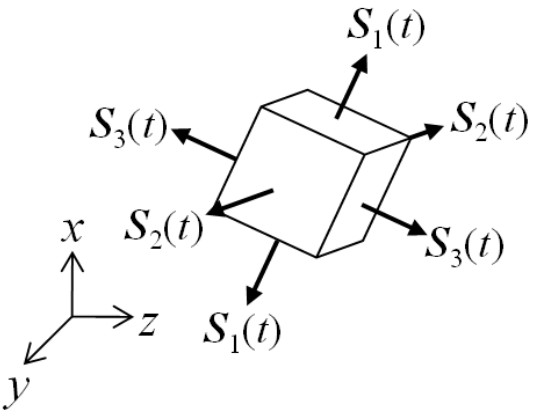

Figure 1: Principal stress and strain in xyz coordinates.

The "Max" denotes taking the larger value from the three in the bracket. The maximum value of $S_I(t)$ during a cycle is defined as the maximum principal value, S_{Imax}, at $t=t_0$ as follows,

$$S_{Imax} = |\boldsymbol{S}_I(t_0)| = \mathrm{Max}\left[\, |\boldsymbol{S}_1(t_0)|,\ |\boldsymbol{S}_2(t_0)|,\ |\boldsymbol{S}_3(t_0)| \,\right] \tag{2}$$

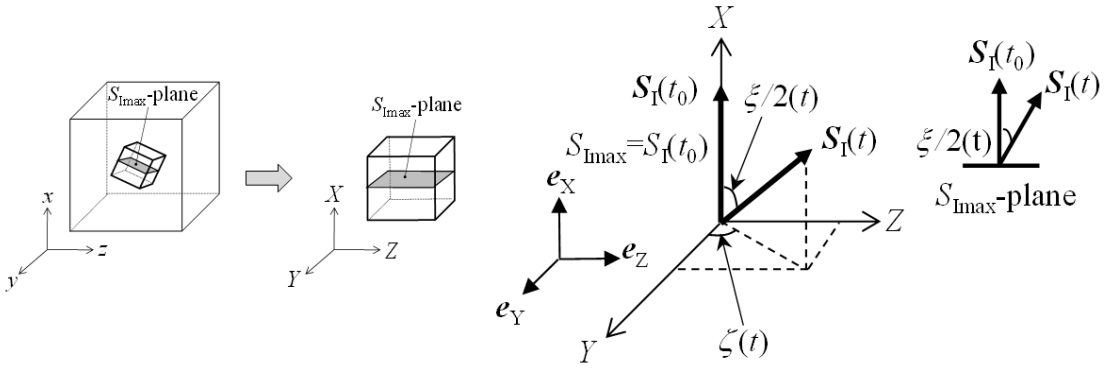

Figure 2: Definition of principal stress and strain directions in XYZ coordinates.

Definition of Principal Stress and Strain Directions

Fig. 2 illustrates two angles, $\xi(t)/2$ and $\zeta(t)$, to express the rotation or direction change of the maximum principal vector, $\boldsymbol{S}_I(t)$, in the new coordinate system of XYZ, where XYZ-coordinates are the material coordinates taking X-axis in the direction of $\boldsymbol{S}_I(t_0)$ with the other two axes in arbitrary directions. The two angles of $\xi(t)/2$ and $\zeta(t)$ are given by

$$\frac{\xi(t)}{2} = \cos^{-1}\left(\frac{\boldsymbol{S}_i(t_0)\ \cdot\ \boldsymbol{S}_i(t)}{|\boldsymbol{S}_i(t_0)|\ |\boldsymbol{S}_i(t)|} \right) \quad \left(0 \le \frac{\xi(t)}{2} \le \frac{\pi}{2}\right) \tag{3}$$

$$\zeta(t) = \tan^{-1}\left(\frac{\boldsymbol{S}_i(t)\cdot \boldsymbol{e}_Z}{\boldsymbol{S}_i(t)\cdot \boldsymbol{e}_Y} \right) \qquad (0 \le \zeta(t) \le 2\pi) \tag{4}$$

where dots in Eqs (3) and (4) denote the inner product and $\boldsymbol{e}_Y$ and $\boldsymbol{e}_Z$ are unit vectors in Y and Z directions, respectively. $\boldsymbol{S}_i(t)$ are the principal vectors of stress or strain used in Eq. (1) and the subscript i takes 1 or 3.

The rotation angle of $\xi(t)/2$ expresses the angle between the $\boldsymbol{S}_I(t_0)$ and $\boldsymbol{S}_I(t)$ directions and the deviation angle of $\zeta(t)$ is the angle of $\boldsymbol{S}_I(t)$ direction from the Y-axis in the X-plane.

Definitions of Stress and Strain in Polar Figure

Fig. 3 shows the trajectory of $\boldsymbol{S}_I(t)$ in 3D polar figure for a cycle where the radius is taken as the value of $\boldsymbol{S}_I(t)$, and the angles of $\xi(t)$ and $\zeta(t)$ are the angles shown in the figure. A new coordinate system is used in Fig. 3 with the three axes of S_I^1, S_I^2 and S_I^3, where S_I^1-axis directs to the direction of $\boldsymbol{S}_I(t_0)$. The rotation angle of $\xi(t)$ has double magnitude compared with that in the specimen shown in Fig. 2 considering the consistency of the angle between the polar figure and the physical plane presentation. The principal range, ΔS_I, is determined as the maximum projection length of $\boldsymbol{S}_I(t)$ on the S_I^1-axis. The mean value, S_{Imean}, is given as the center of the range. ΔS_I and S_{Imean} are equated as,

$$\Delta S_I = \mathrm{Max}\left[S_{Imax} - \cos\xi(t)\ S_I(t) \right] = S_{Imax} - S_{Imin} \tag{5}$$

$$S_{Imean} = \frac{1}{2}\left(S_{Imax} + S_{Imin} \right) \tag{6}$$

S_{Imin} is the $S_I(t)$ to maximize the value of the bracket in Eq. (5). The sign of S_{Imin} in the figure is set to be positive if it does not cross the S_I^2-S_I^3 plane and the sign negative if it crosses the plane.

The advantage of the definitions of the maximum principal range and mean value above mentioned is that the two are determinable without human judgments for any loading case in 3D stress and strain space. The range and mean value are consistent used in simple loading cases which are discussed in the case studies in the followings. $S_I(t)$ can be replaced by equivalent values of stress or strains, such as the von Mises and the Tresca, in case of necessity from user's requirement.

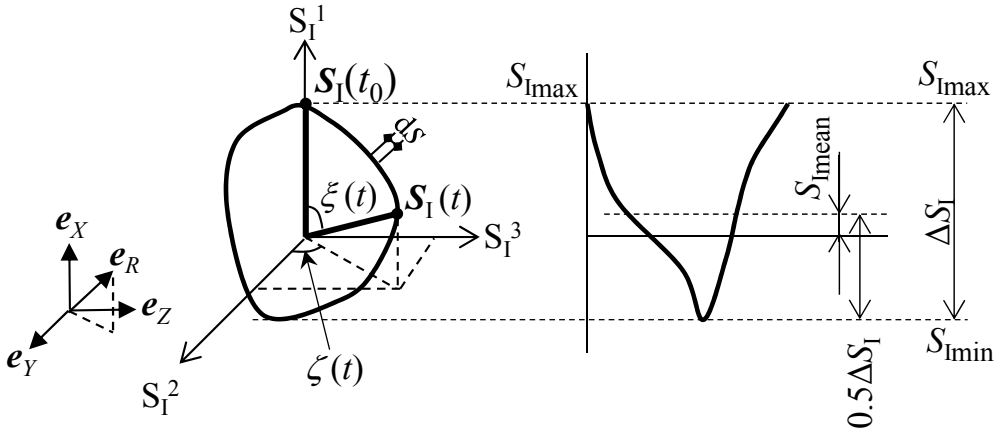

Figure 3: Definition of principal range and mean principal value.

CASE STUDIES

This section discusses a couple of case studies for ΔS_I and S_{Imean} under proportional and non-proportional loadings under biaxial plane stress condition. The symbol S takes (ε) in the case studies in the followings.

Proportional loading

Fig. 4 (a) illustrates three proportional strain paths for normal and shear strainings under plane stress condition in the normal strain – shear strain (ε–$\gamma/\sqrt{3}$) plot. The path A-A' is push-pull loading, the B-B' combined tension and shear loading and the path C-C' shear loading. Figs 4 (b)–(d) show the variations of $\varepsilon_1(t)$, $\varepsilon_3(t)$, $\varepsilon_I(t)$, $\xi(t)/2$ and $\zeta(t)$ and Fig. 4 (e) the strain path in the polar figure presentation.

Principal strains and their angle change are obtained in the stages of OA-OB-OC and OA'-OB'-OC' as follows.

Stage OA-OB-OC:

$$\left.\begin{matrix}\varepsilon_1(t)\\ \varepsilon_2(t)=\varepsilon_3(t)\end{matrix}\right\}=\frac{1-\nu}{2}\varepsilon\pm\frac{1}{2}\sqrt{(1+\nu)^2\varepsilon^2+\gamma^2}$$

$$\varepsilon_1(t)=\varepsilon_1(t) \quad Since\ of\ \varepsilon_1(t)\geq|\varepsilon_3(t)| \tag{7.a}$$

$$\varepsilon_{Imax}=\varepsilon_I(k) \quad k=A,\ B\ or\ C$$

$$\xi(t)=0°,\quad \zeta(t)=0^\circ$$

Stage OA'-OB'-OC':

$$\left.\begin{matrix}\varepsilon_1(t)=\varepsilon_2(t)\\ \varepsilon_3(t)\end{matrix}\right\}=\frac{1-\nu}{2}\varepsilon\pm\frac{1}{2}\sqrt{(1+\nu)^2\varepsilon^2+\gamma^2}$$

$$\varepsilon_1(t)=|\varepsilon_3(t)| \quad Since\ of\ \varepsilon_1(t)\leq|\varepsilon_3(t)| \tag{7.b}$$

$$\xi(t)=180°,\quad \zeta(t)=0^\circ$$

ν is the Poisson's ratio. Note that $\gamma/\sqrt{3}$=0 in the loading stages of OA and OA' and ε=0 in the loading stages of OC and OC'.

The maximum principal strains ($\varepsilon_1(t)$) vary along the solid lines in Fig. 4 (b) in the loading stages of OA, OB and OC, and the minimum principal strains ($\varepsilon_3(t)$) along the dashed lines in the same loading stages. In these cases, the maximum principal strains all have a positive sign, whereas the minimum principal strains a negative sign. $\varepsilon_I(t)$ makes the positive triangle waveforms as illustrated in Fig. 4 (c) because $\varepsilon_I(t)$ is either $\varepsilon_1(t)$ or $\varepsilon_3(t)$ taking larger absolute strain as shown in Eq. (1). The principal strain, $\varepsilon_I(t)$, changes its direction by an angle of 180° (ξ/2=90°) at the origin O in the reversed

loading stages of AA', BB' and CC', Fig. 4 (d). Finally, the straight loading lines are obtained in the polar figure as shown in Fig. 4 (e). In the proportional loadings in Fig. 4 (a), the directions of $\varepsilon_I(t)$ are fixed (ξ=0 or 180°) and ζ=0°.
The maximum strain range and mean strain are expressed as

$$\Delta\varepsilon_I = \varepsilon_{I\max} + \varepsilon_{I\min} = \varepsilon_1(k) - \varepsilon_3(k') \tag{8}$$

$$\varepsilon_{I\mathrm{mean}} = \frac{1}{2}\left(\varepsilon_{I\max} - \varepsilon_{I\min}\right) = \frac{1}{2}\left(\varepsilon_1(k) + \varepsilon_3(k')\right) \tag{9}$$

as shown in Fig. 4 (e), where k takes A, B or C and k' A', B' and C'. The results agree well with the principal strain range and mean strain we have considered by putting a sign with human operation.

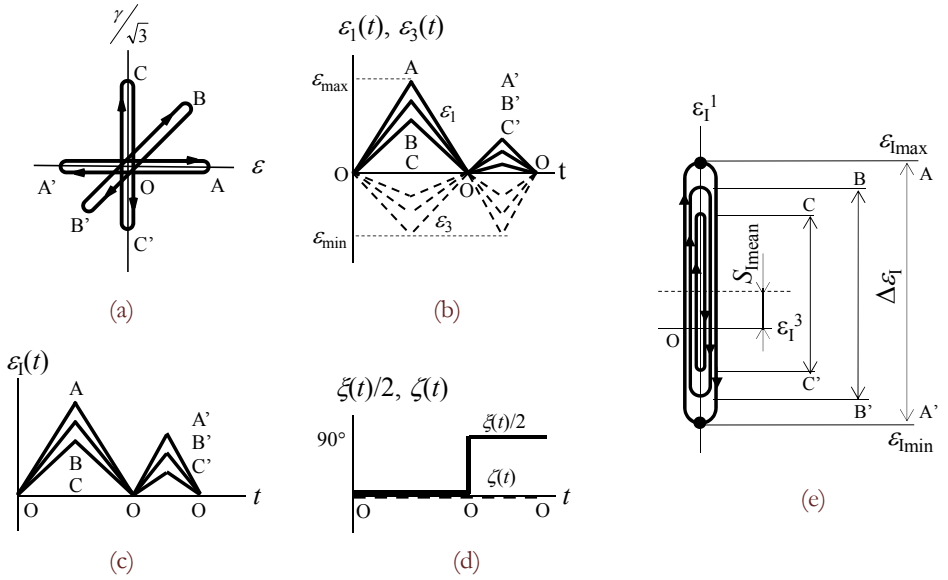

Figure 4: Variations of ε_i(t), $\varepsilon_I(t)$ and $\xi(t)/2$ in proportional straining: (a) Strain paths on $\varepsilon-\gamma/\sqrt{3}$ plot, (b) Variation of $\varepsilon_i(t)$, (c) Variation of $\varepsilon_I(t)$, (d) Variation of $\xi(t)$ and $\zeta(t)$, (e) Strain paths on polar figure.

Non-proportional Loading

Fig. 5 shows non-proportional loading cases of the cruciform and box shapes. In the figure, $\varepsilon_{I\max}$ is assumed to be given by ε_I(A) and ε_I(a) in the cruciform and box shape loadings, respectively. The principal strains and the direction of $\varepsilon_I(t)$ in each stage in the figure are expressed as follows.
Principal strains:
Stage OA, OB, OD and DdAaB

$$\left.\begin{array}{l}\varepsilon_1(t)\\ \varepsilon_2(t)=\varepsilon_3(t)\end{array}\right\} = \frac{1-\nu}{2}\varepsilon \pm \frac{1}{2}\sqrt{(1+\nu)^2\varepsilon^2+\gamma^2}$$
$$\varepsilon_1(t)=\varepsilon_1(t) \quad \textit{Since of } \varepsilon_1(t) \geq \left|\varepsilon_3(t)\right| \tag{10.a}$$
$$\varepsilon_{I\max}=\varepsilon_I(\mathrm{A})=\varepsilon_1(\mathrm{A}) \quad \textit{for cruciform loading}$$
$$\varepsilon_{I\max}=\varepsilon_I(\mathrm{a})=\varepsilon_1(\mathrm{a}) \quad \textit{for box-shaped loading}$$

Stage OC and BbCcD

$$\left.\begin{array}{l}\varepsilon_1(t)\\ \varepsilon_2(t)=\varepsilon_3(t)\end{array}\right\} = \frac{1-\nu}{2}\varepsilon \pm \frac{1}{2}\sqrt{(1+\nu)^2\varepsilon^2+\gamma^2}$$
$$\varepsilon_I(t)=\left|\varepsilon_3(t)\right| \quad \textit{Since of } \varepsilon_1(t) \leq \left|\varepsilon_3(t)\right| \tag{10.b}$$

Direction of $\varepsilon_I(t)$:

Stage OA, OB, OD for cruciform loading

$$\xi(t)=0°,\ \zeta(t)=0° \quad along \quad OA$$
$$\xi(t)=90°,\ \zeta(t)=90° \quad along \quad OB \qquad (11.a$$
$$\xi(t)=90°,\ \zeta(t)=-90° \quad along \quad OD$$

Stage OC for cruciform loading

$$\xi(t)=180°,\ \zeta(t)=0° \quad along \quad OC \qquad (11.b)$$

Stage aBbCc for box-shaped loading

$$0\le\xi(t)\le 180°,\ \zeta(t)=90° \qquad (11.c)$$

Stage cDdAa for box-shaped loading

$$0\le\xi(t)\le 180°,\ \zeta(t)=-90° \qquad (11.d)$$

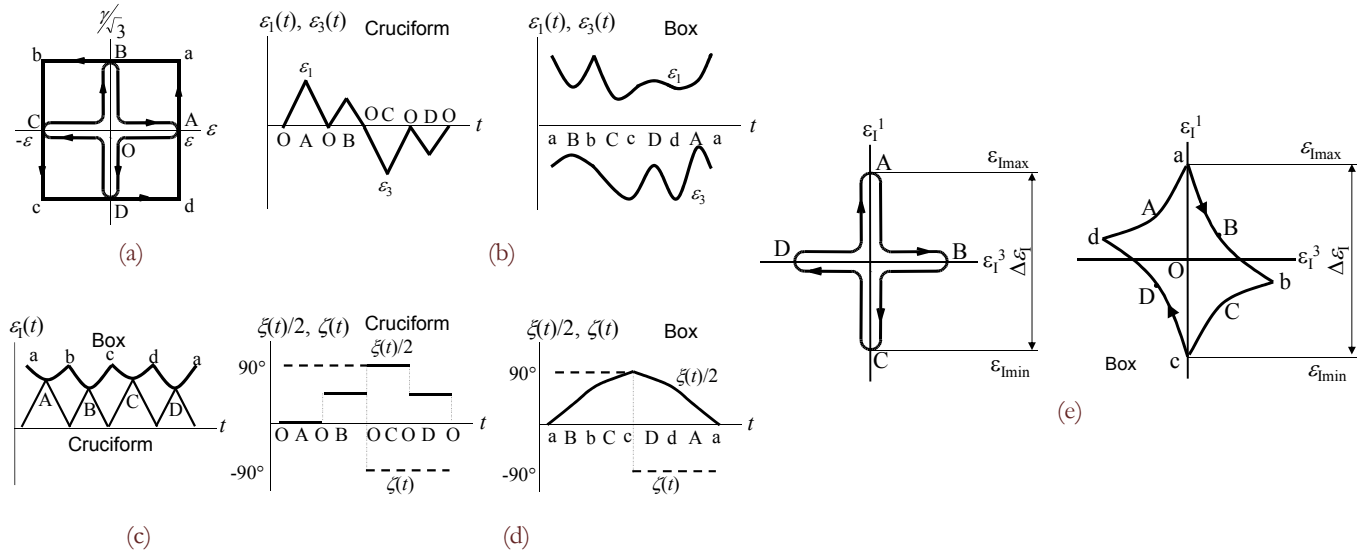

Figure 5: Variations of ε_i(t), $\varepsilon_I(t)$ and $\xi(t)/2$ in non-proportional straining: (a) Strain paths on $\varepsilon-\gamma/\sqrt{3}$ plot, (b) Variation of $\varepsilon_i(t)$, (c) Variation of $\varepsilon_I(t)$, (d) Variation of $\xi(t)$ and $\zeta(t)$, (e) Strain paths on polar figure.

In the cruciform loading, $\varepsilon_I(t)$ makes four triangles shown in Figs 5 (b) and (c). The angle of $\xi(t)$ rotates in the range of $0\le\xi(t)\le180°$, Fig. 5 (d), and the angle of $\zeta(t)$ changes by 90° at the origin O in a cycle. The principal strain path in the polar figure became a cruciform shape as shown in Fig. 5 (e).

In the box loading, $\varepsilon_1(t)$ takes positive and $\varepsilon_3(t)$ negative values without changing sign in a cycle as shown in Fig. 5 (b). Then, $\varepsilon_I(t)$ in the box loading has large mean value with a small fluctuation during a cycle, Fig. 5 (c). The principal strain direction rotates continually in the range of $0\le\xi(t)\le180°$ and $\zeta(t)=\pm90°$ and the principal strain path forms rhombus shape, Figs 5 (d) and (e).

The maximum strain ranges are

$$\Delta\varepsilon_I=\varepsilon_{I\max}+\varepsilon_{I\min}=\varepsilon_1(\mathrm{A})-\varepsilon_3(\mathrm{C}) \quad for\ cruciform\ loading \qquad (12.a)$$

$$\Delta\varepsilon_I=\varepsilon_{I\max}+\varepsilon_{I\min}=\varepsilon_1(\mathrm{a})-\varepsilon_3(\mathrm{c}) \quad for\ box\text{-}shaped\ loading \qquad (12.b)$$

The mean strain in the two cases is 0.

DEFINITION OF NON-PROPORTIONALITY

The authors proposed the non-proportional strain range expressed in Eq. (13) for correlating MLCF lives under non-proportional loading [6, 7, 11-14].

$$\Delta\varepsilon_{NP} = \left(1 + \alpha f_{NP} \right) \Delta\varepsilon_{I} \tag{13}$$

In the equation, $\Delta\varepsilon_I$ is the principal strain range discussed previously. α is a material constant expressing the amount of additional hardening by non-proportional loading and is defined as the ratio of a saturated principal stress in the circular loading to that in uniaxial push-pull loading at the same principal strain amplitude for additional hardening material. In Eq. (13), $\Delta\varepsilon_I$ also can be replaced by the other equivalent stains based on the user's requirement although trends of data correlation are different between the strains used which have been discussed in other studies [6, 7, 11-14].
f_{NP} is the non-proportional factor that expresses the severity of non-proportional loading in the form as [6, 7, 11-14],

$$f_{NP} = \frac{b}{\mathrm{T}\,\varepsilon_{\mathrm{I}\max}} \int_0^T \left(\left| \sin\left(\xi(t)\right) \right| \varepsilon_{\mathrm{I}}(t) \right) dt \tag{14}$$

where T is the time for a cycle. b is a constant for making f_{NP}=1 in the circular loading on ε–$\gamma/\sqrt{3}$ plot and b takes $\pi/2$ when $\varepsilon_I(t)$ is employed [6, 7]. In Eq. (14), f_{NP} is calculated by measuring the rotation of the maximum principal strain direction and the integration the strain amplitude after the rotation. Therefore, f_{NP} evaluates comprehensively the severity of non-proportional cyclic loading based on the amplitude of strain and the direction change of principal strain.
This paper proposes a modified non-proportional factor, f'_{NP}, to be applicable for 3D stress and strain space defined in chapter 3, which is expressed as,

$$f'_{NP} = \frac{\pi}{2\, S_{\mathrm{I}\max}\, L_{\mathrm{path}}} \int_C |\boldsymbol{e}_{\mathrm{I}} \times \boldsymbol{e}_{\mathrm{R}}|\, S_{\mathrm{I}}(t)\, \mathrm{d}s$$
$$L_{\mathrm{path}} = \int_C \mathrm{d}s \tag{15}$$

where $\boldsymbol{e}_R$ is a unit vector directing to $\boldsymbol{S}_I(t)$, ds the infinitesimal trajectory of the loading path shown in Fig. 3. L_{path} is the whole loading path length during a cycle and "×" denotes vector product. The scalars, S_{Imax} and L_{path}, before the integration in Eq. (15) is set to make f'_{NP} unity in the circler loading in 3D polar figure. Integrating the product of amplitude and principal direction change of stress and strain by path length in Eq. (15) is more suitable for evaluation of fatigue damage rather than the integration by time.

Type	1	2	3	4	5	6
Loading path	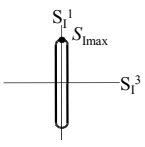	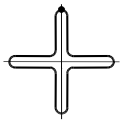	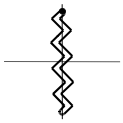		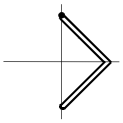	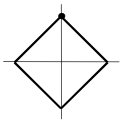
f_{NP}	0	0.39	0.10	0.20	0.79	0.79
f'_{NP}	0	0.49	0.12	0.24	0.71	0.71
Type	7	8	9	10	11	12
Loading path	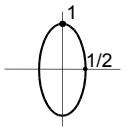	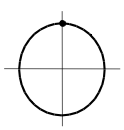	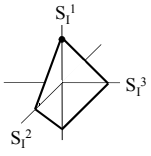		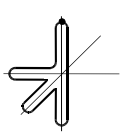	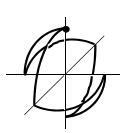
f_{NP}	0.53	1.06	-	-	-	-
f'_{NP}	0.5	1	0.71	0.98	0.49	1.78

Figure 6: Comparing f_{NP} and f'_{NP} under several loadings.

Fig. 6 compares the values of f_{NP} with those of f'_{NP} for several loading paths for the case of strain. Small difference in the value between f_{NP} and f'_{NP} is found because of different definition between them. However, f'_{NP} has the advantages applicable to 3D stress and strain conditions.

Fig. 7 shows a flow chart of calculation of stress or strain range and non-proportionality. When 6 components of stress or strain at time t as the data obtained from experiment, numerical analysis such as a finite element analysis or *etc.*, ΔS_I and f'_{NP} are calculated based on the procedures presented in above. Then, evaluation of fatigue damage can be analyzed by user's method or Itoh-Sakane model [13].

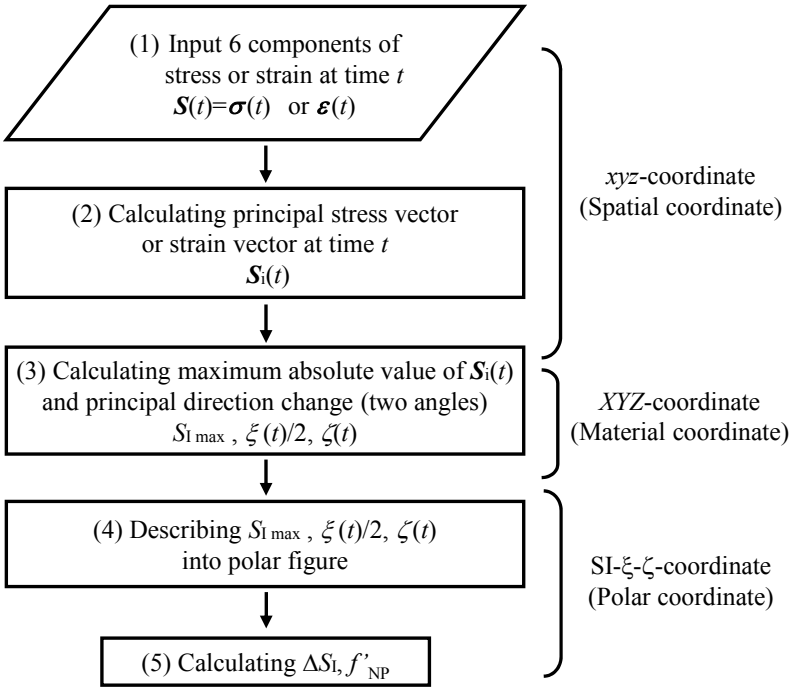

Figure 7: Flow chart of calculation of stress or strain range and non-proportionality.

NON-PROPORTIONAL STRESS AND STRAIN RANGES FOR LIFE EVALUATION

The authors analyzed the non-proportional LCF lives of type 304 steel tube specimens fatigued using 15 strain waveforms shown in Fig. 8 at 923 K [22]. Figs 9 (a)–(c) correlate non-proportional fatigue lives with the ASME equivalent strain range ($\Delta\varepsilon_{ASME}$) and two maximum stress ranges of $\Delta\sigma_I^e$ and $\Delta\sigma_I$. $\Delta\varepsilon_{ASME}$ is the strain range based on Mises equivalent strain and is the strain range recommended in the Code Case of ASME, Section III, Division 1 NH [1]. $\Delta\sigma_I^e$ is the principal stress range calculated from $\Delta\varepsilon_I$ multiplied by Young's modulus of 145 GPa. The correlation using $\Delta\sigma_I^e$ was made considering that conventional design usually uses stress ranges elastically calculated from strain ranges. $\Delta\sigma_I$ is the maximum principal stress range experimentally obtained at $1/2N_f$. In the figures, heavy solid lines are drawn based on the Case 0 data and two thin solid lines show a factor of 2 scatter band.

Fig. 9 (a) clearly indicates that $\Delta\varepsilon_{ASME}$ overestimates the non-proportional fatigue lives in the cases with sever non-proportionalities. For type 304 stainless steel at room temperature, the more drastic reduction in LCF lives due to non-proportional loading beyond a factor of 10 was also reported [4, 5, 7, 12, 15]. The cause of the overestimates results from that $\Delta\varepsilon_{ASME}$ does not cover the effect of non-proportional loading on life. The correlation with $\Delta\sigma_I^e$ shown in Fig. 9 (b) appears to be a similar trend to that in Fig. 9 (a). $\Delta\sigma_I^e$ has larger magnitude than experimental practically because the stress was calculated elastically even in plastic deformation occurred. In the data correlation with $\Delta\sigma_I$, Fig. 9 (c), LCF lives under non-proportional loading are underestimated. The underestimate of the LCF lives under non-proportional loading may result from the additional hardening due to non-proportional loading, because $\Delta\sigma_I$ does not cover the additional hardening due to non-proportional loading resulting in reduction in life.

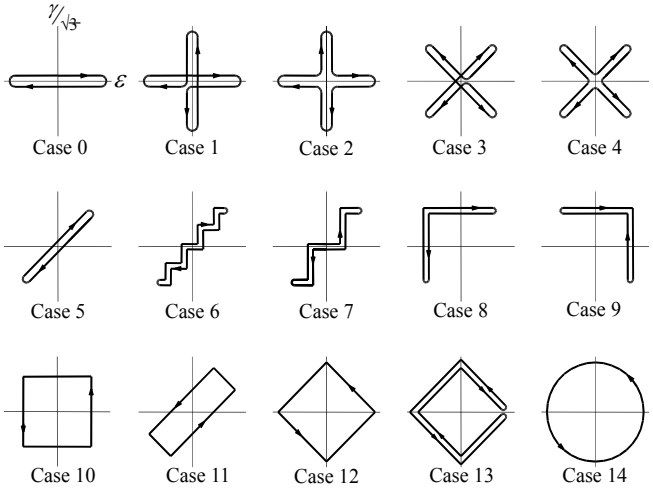

Figure 8: 15 strain paths employed in the non-proportional LCF test.

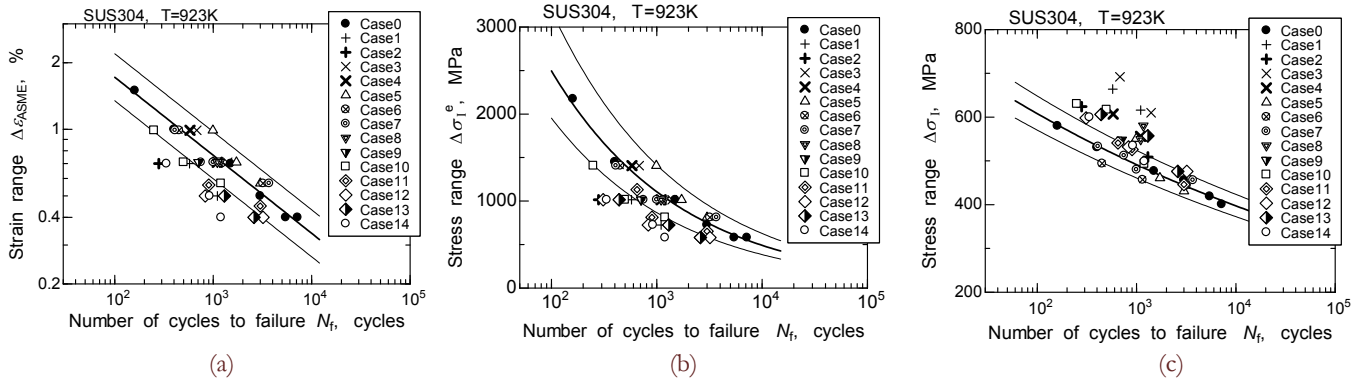

Figure 9: Correlation of non-proportional LCF lives with $\Delta\varepsilon_{ASME}$, $\Delta\sigma_I^e$ and $\Delta\sigma_I$: (a) $\Delta\varepsilon_{ASME} - N_f$, (b) $\Delta\sigma_I^e - N_f$, (c) $\Delta\sigma_I - N_f$.

Fig. 10 correlates the non-proportional LCF lives with $\Delta\varepsilon_{NP}$, where material constant, α, is set to 0.4. $\Delta\varepsilon_{NP}$ correlates the non-proportional fatigue lives with a small scatter. α employed was determined from the degree of additional hardening. This result suggests that a suitable strain parameter for multiaxial LCF life evaluation must take account of intensity of non-proportionality of loading and additional hardening due to non-proportional loading. The former is the non-proportional factor, f_{NP} or f'_{NP}, and the latter is the material constant, α, in $\Delta\varepsilon_{NP}$.

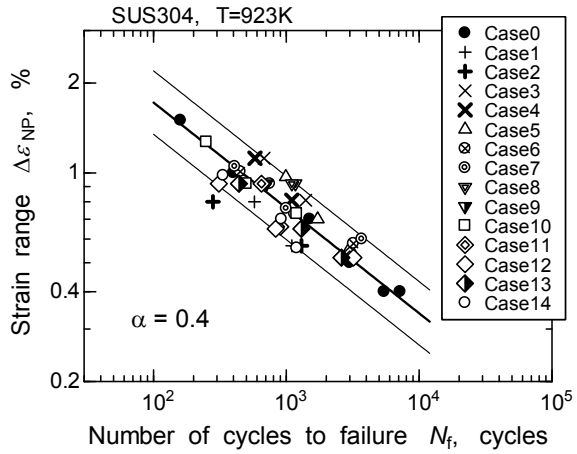

Figure 10: Correlation of non-proportional LCF lives with $\Delta\varepsilon_{NP}$.

VISUALIZATIONS AND ANALYSES OF STRESS AND STRAIN STATE AND LIFE EVALUATION

Outline of Program for Visualization

Based on the definition of stress and strain mentioned above, a program is developed to analyze and visualize stress/strain and evaluate the failure life under non-proportional loading. The programming code used is C#. Fig. 11 is a flowchart of the program, which is divided into 8 categories as below.

(1) Input data

The stress/strain data *vs.* time obtained from experimental or calculated result, denoted by $\boldsymbol{S}(t)$, is read into the program. The input data consists of the 6 components of stress/strain and time at each column. Additional columns (temperature, pressure, *etc.*) can be added. As an example, for a butterfly-shape strain path under the combined push-pull and cyclic reversed torsion loadings using a hollow cylinder specimen, Figs. 12 (a) and (b) show a strain path in ε–$\gamma/2$ plot and a strain path in polar figure coordinates, respectively, where ε and γ are the total axial and the total shear strains. In the figures, attached characters 'A-C' will be referenced later. Fig. 13 is the table of the input data formatted for the program.

(2) Calculation of $\boldsymbol{S}_{\mathrm{I}}(t)$ and $\boldsymbol{S}_{\mathrm{Imax}}$

In this step, $\boldsymbol{S}_{\mathrm{I}}(t)$ and $\boldsymbol{S}_{\mathrm{Imax}}$ are calculated in accordance with the IS-method.

(3) Determination of reference axis

The reference axis for defining $\xi(t)$ and $\zeta(t)$ is determined. The determination of the reference axis has three methods (Method-1, -2 and -3). In Method-1, the reference axis corresponds to the direction of S_{Imax}, which is the maximum amplitude of stress/strain in a cycle. In Method-2, the reference direction is put into the direction perpendicular to a critical plane defined as critical plane approach [23, 24]. In this study, the critical plane is determined as the plane where cumulative normal stress/strain becomes the maximum in a cycle under the random loading. In Method-3, users can define the reference axis as any direction at their request. The reference axes determined by Method-1, -2 and -3 are denoted by the characters A, B and C, respectively, in Fig. 12.

(4) Calculation of $\xi(t)$ and $\zeta(t)$

In accordance with the IS-method, calculations of $\xi(t)$ and $\zeta(t)$, etc. are carried out.

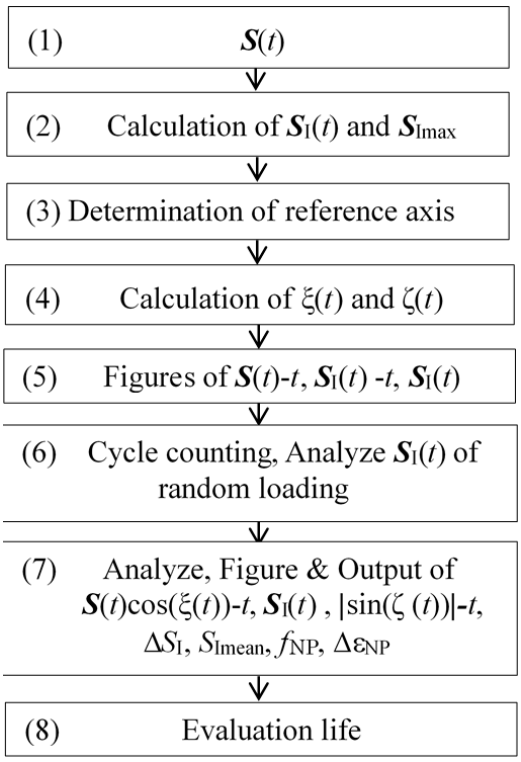

Figure 11: Calculation flow in the program.

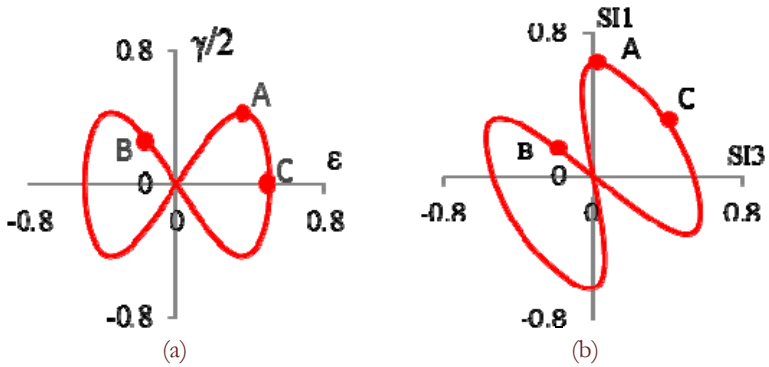

Figure 12: 4 Strain paths of input data: (a) In ε-γ/2 plot. (b) In polar figure.

	A	B	C	D	E	F	G	H
1	2013/8/5							
2	University of Fukui, Proposer							
3	Time(s)	temp(D)	Strain()					
4	0	25	0	0	0	0	0	0
5	1	25	0.0868	−0.02604	−0.02604	0.2962	0	0
6	2	25	0.171	−0.0513	−0.0513	0.5566	0	0
7	3	25	0.25	−0.075	−0.075	0.75	0	0
8	⋮	⋮	⋮	⋮	⋮	⋮	⋮	⋮
9	⋮	⋮	⋮	⋮	⋮	⋮	⋮	⋮
10	9	25	0.5	−0.15	−0.15	0	0	0
11	10	25	0.4924	−0.14772	−0.14772	−0.2962	0	0
12	11	25	0.4698	−0.14094	−0.14094	−0.5566	0	0
13	⋮	⋮	⋮	⋮	⋮	⋮	⋮	⋮
14	⋮	⋮	⋮	⋮	⋮	⋮	⋮	⋮

Figure 13: Formatted input data.

(5) Figures of $\boldsymbol{S}(t)$-t, $\boldsymbol{S}_I(t)$-t and $\boldsymbol{S}_I(t)$-$\xi(t)$-$\zeta(t)$

By the calculations and analyses in the above categories, descriptions of $\boldsymbol{S}(t)$-t, $\boldsymbol{S}_I(t)$-t and $\boldsymbol{S}_I(t)$-$\xi(t)$-$\zeta(t)$ are calculated. Fig. 14 shows a graph of the input data for strains, as a function of time, shown in Figs. 12 and 13. Figs. 15 (a) and (b) illustrate the strain path in the polar coordinates, *i.e.*, $\boldsymbol{S}_I(t)$-$\xi(t)$-$\zeta(t)$ and the projection of $\boldsymbol{S}_I(t)$ and non-proportionality of loading as a function of time t. In Fig. 15 (a), attached characters, A, B and C, indicate the directions of the reference axes. Tab. 1 shows results as output data and they are strain ranges and non-proportional factors evaluated for each reference axis assuming the axial strain range $\Delta\varepsilon$=1.0%.

(6) Cycle counting and analysis of $\boldsymbol{S}_I(t)$ for random loading

Under the random loading, waveform of stress/strain must be analyzed using a counting method, such as a rain-flow counting method, and damage also has to be evaluated by a cumulative damage rule like Miner's rule. Stress/strain waveform under non-proportional loading was already reduced to the simple waveform in the categories (1)-(5), the cycle counting and the cumulative damage rule used in uniaxial loading can be applied to the non-proportional loading.

(7) Figure and output of results evaluated by the program

In this step, all the figures and tables can be graphed and saved to memory. By examining the figures, the users can visually understand the multiaxiality and non-proportionality of stress/strain state simultaneously.

(8) Damage and life evaluation

Based on the results obtained in the categories (1)-(7), failure life evaluation can be performed. For the life evaluation, S-N curve base data and the IS-method are employed with the rain-flow cycle counting method and cumulative damage rule.

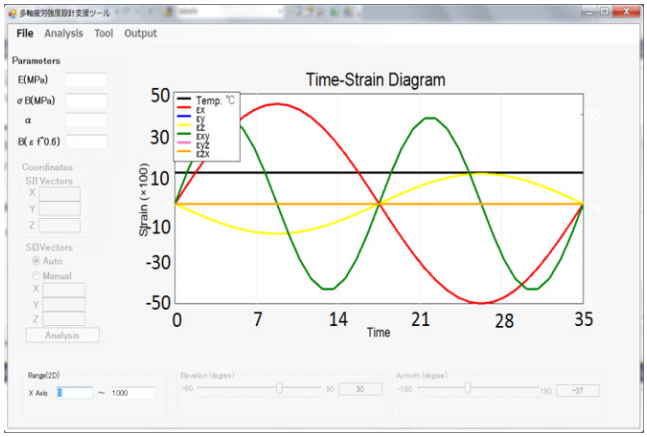

Figure 14: Strain waveforms of input data.

Method	1	2	3
Reference axis	OA	OB	OC
$\Delta\varepsilon_I$	1.26	1.24	1.09
f_{NP}	0.65	0.66	0.78
$\Delta\varepsilon_{NP}$	1.87	1.85	1.42

Table 1: Comparison of evaluated parameters.

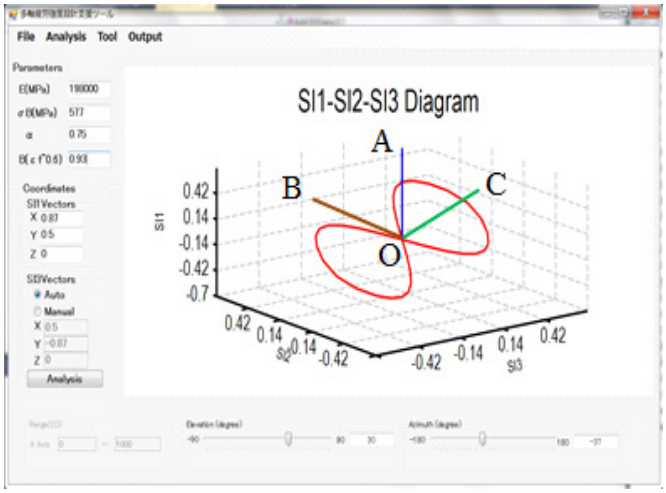

(a)

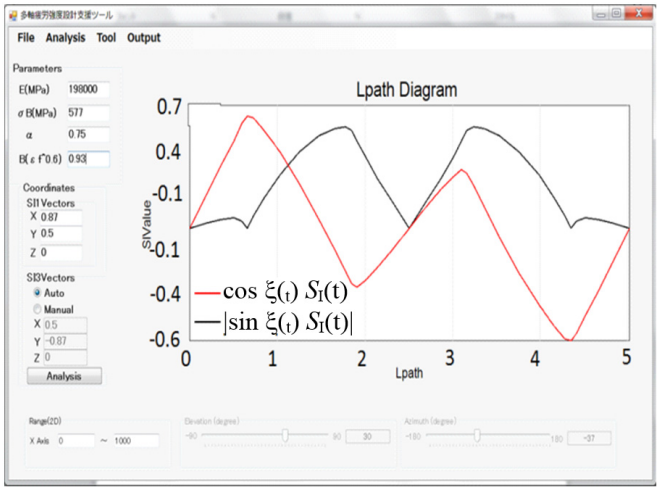

(b)

Figure 15: Output strain path in polar coordinates and waveforms: (a) Strain path in polar coordinates. (b) Strain waveforms projected to reference axis.

Life Evaluation under Random Loading

One example of life evaluation under random loading is presented here. Material used is a rolled steel for general structure, type SS400, whose material properties are; Yong's modulus E=206 GPa, tensile strength σ_B=437 MPa. The failure life curve employed for evaluation is given by Eq.(16), which is obtained from experiment.

$$\Delta\sigma = -69\log_e N_f + 1190 \tag{16}$$

Figs. 16 (a) and (b) show stress waveforms of the input data for 1 block cycles and the calculated stress path in the polar coordinates, respectively. It is clear that the evaluated stress path is proportional loading since the stress path in Fig. 15 (b) is shown by a unique straight line. Counting method employed was a rain-flow method and 1 block was counted as 30,000 cycles. Tab. 2 shows the numerical values of fatigue damage and evaluated life by using a linear cumulative damage low. This analysis was carried out by using the test results under proportional loading, so more discussion about the applicability of the program to the evaluation of fatigue strength under non-proportional loading will be studied after the experimental results under non-proportional loading are obtained. Under the non-proportional loading, especially definition of non-proportionality will be required. In there, f_{NP} will be calculated at each separate stress amplitude obtained by the counting method.

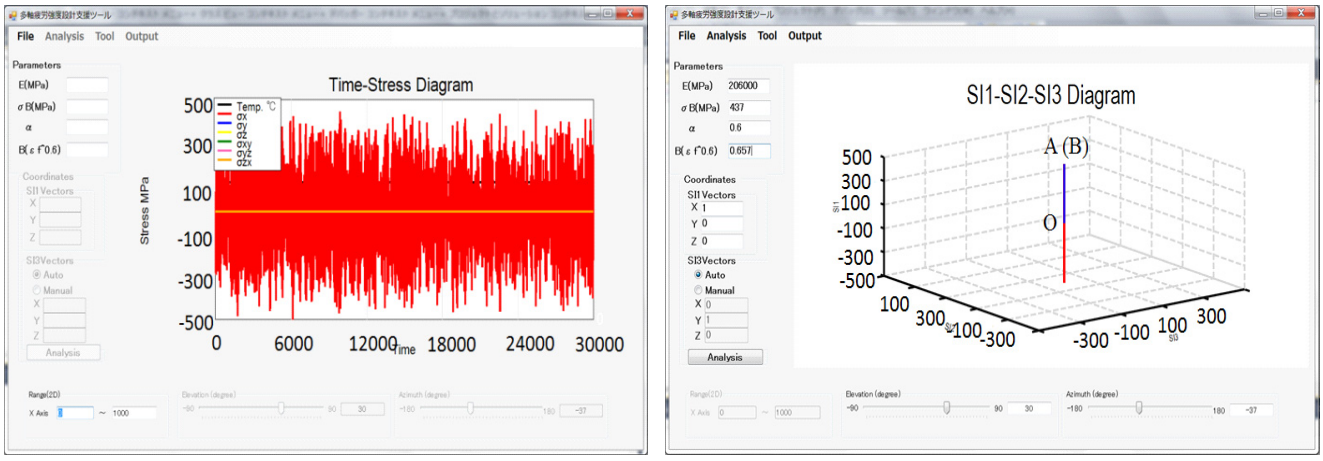

(a) (b)

Figure 8: Input and output data under random loading: (a) Input data, (b) Output data in polar coordinates.

Reference axis	OA (OB)
σ_{max} (MPa)	447
Damage per block	0.161
Evaluated life (blocks)	6
Experimental life (blocks)	8

Table 2: Life evaluation under random loading.

CONCLUSIONS

1. This paper proposed a simple method of determining the principal stress and strain ranges together with the mean stress and strain under proportional and non-proportional loading in 3D stress and strain space. It also proposed the method of defining the rotation and deviation angles of the maximum principal stress and strain.
2. The paper extend the non-proportional factor, f_{NP}, from 2D to 3D stress and strain space with the consistency with the previous definition of it in the 2D space.

3. Applicability of the non-proportional strain was discussed for describing the high temperature proportional and non-proportional low cycle fatigue lives.
4. Based on the IS-method to evaluate stress/strain and failure life under non-proportional loading, this study developed a program for visually presenting the stress/strain state, the non-proportionality of loading, and the damage evaluation. It is possible for researchers and engineers to assess the fatigue strength under non-proportional loading without requiring special knowledge and judgment about multiaxial loading.

REFERENCES

[1] ASME, Boiler and Pressure Vessel Code Section III, Division 1 NH (2004).
[2] ASME, Boiler and Pressure Vessel Code Section VIII, Division 3 (2004).
[3] Fatemi, A., Socie, D.F., A critical plane approach to multiaxial fatigue damage including out-of-phase loading, Fatigue Fract Engng Mater Struct, 11(3) (1988) 149-165.
[4] Nitta, A., Ogata, T., Kuwabara, K., Fracture modes and fatigue life evaluation of SUS 304 stainless steel under non-proportional biaxial loading conditions, J Society Material Science, Japan, 38(427) (1989) 416-422.
[5] Doong, S.H., Socie, D.F., Robertson, I.M., Dislocation substructures and nonproportional hardening, Trans ASME, J Engng Mater Technol, 112 (1990) 456-565.
[6] Itoh, T., Sakane, M., Ohnami, M., Socie, D.F., Nonproportional low cycle fatigue criterion for type 304 stainless steel, Trans ASME, J Engng Mater Technol, 117 (1995) 285-292.
[7] Itoh, T., Nakata, T., Sakane, M., Ohnami, M., Non-proportional low cycle fatigue of 6061 aluminum alloy under 14 strain path, Multiaxial Fatigue and Fracture (Macha *et al.*, eds.), ESIS-25, (1999) 41-54.
[8] Socie, D.F., Marquis G., *eds*, 'Multiaxial Fatigue', SAE International (2000).
[9] Smith, R.N., Watson, P., Topper, T.H., A stress-strain parameter for the fatigue of metals, J Materials, 5(4) (1970) 767-778.
[10] Shamsaei, N., Fatemi, A., Socie, D.F., Multiaxial fatigue evaluation using discriminating strain paths, Int J Fatigue, 33(4) (2011) 597-609.
[11] Itoh, T., Effect of direction change in maximum principal strain axis on multiaxial low cycle fatigue life of type 304 stainless steel at elevated temperature, J Society Material Science, Japan, 49(9) (2000) 988-993.
[12] Itoh, T., A model for evaluation of low cycle fatigue lives under non-proportional straining, J Society Material Science, Japan, 50(12) (2001) 1317-1322.
[13] Itoh, T., Sakane, M., Hata, T., Hamada, N., A design procedure for assessing low cycle fatigue life under proportional and non-proportional loading, Int J Fatigue, 28(8) (2006) 495-466.
[14] Itoh, T., Sakane, M., Ozaki, T., Determination of strain and stress ranges under cyclic proportional and non-proportional loading, J Society Material Science, Japan, 60(2) (2011) 88-93.
[15] Itoh, T., Yang, T., Material dependence of multiaxial low cycle fatigue lives under non-proportional loading, Int J Fatigue, 33(8) (2011) 1025-1031.
[16] Ogata, T., Nitta, A., Evaluation of multiaxial low-cycle fatigue failure based on new criterion and its application to high temperature structural design, J Society Material Science, Japan, 42(472) (1993) 72-77.
[17] Kobayashi, M., Ohno, N., Igari, T., Thermal ratcheting analysis of cylinders subjected to axial travelling of temperature distribution: comparison with experiments of 316FR steel cylinders, J Society Material Science, Japan, 46(8) (1997) 906-913.
[18] Aoto, K., Structural materials development for sodium cooled fast reactor, Materia Japan, 47(9) (2008) 459-463.
[19] Sakane, M., Ohnami, M., Sawada, M., Fracture modes and low cycle biaxial fatigue life at elevated temperature, Trans ASME, J Engng Mater Technol, 109 (1987) 236-242.
[20] Sakane, M., Ohnami, M., Hamada, N., Biaxial low cycle fatigue for notched, cracked, and smooth specimens at high temperature, Trans ASME, J Engng Mater Technol, 110 (1988) 48-54.
[21] Itoh, T., Sakane, M., Ohnami, M., High temperature multiaxial low cycle fatigue of cruciform specimen, Trans ASME, J Engng Mater Technol, 116 (1994) 90-98.
[22] Hamada, N., Sakane, M., High temperature nonproportional low cycle fatigue using fifteen loading paths, Proceedings of 5th int. conf. on Biaxial/Multiaxial Fatigue and Fracture, 1 (1997) 251-266.
[23] Socie, D.F., Multiaxial fatigue damage models, Journal of Engineering Materials and Technology, 109 (1987) 293-298.
[24] Fatemi, A., Socie, D.F., A critical plane approach to multiaxial fatigue damage including out-of-phase loading, Fatigue & Fracture of Engineering Materials & Structures, 11(3) (1988) 149-165.